Journal of CO2 Utilization 80 (2024) 102692

Contents lists available at ScienceDirect

Journal of CO2 Utilization

journal homepage: www.elsevier.com/locate/jcou

Systematic screening of transition-metal-doped hydroxyapatite for efficient photocatalytic CO_2 reduction

Yuting Li [a,b], Daniel Bahamon [a], Josep Albero [c], Núria López [b,*], Lourdes F. Vega [a,*]

[a] Research and Innovation Center on CO2 and Hydrogen (RICH Center) and Chemical and Petroleum Engineering Department, Khalifa University, PO Box 127788, Abu Dhabi, UAE
[b] Institute of Chemical Research of Catalonia (ICIQ), The Barcelona Institute of Science and Technology (BIST), Països Catalans 16, 43007 Tarragona, Spain
[c] Instituto Universitario de Tecnología Química (CSIC-UPV), Universitat Politècnica de València, Avda. de los Naranjos s/n, 46022 València, Spain

ARTICLE INFO

Keywords:
CO_2 photoreduction
Density Functional Theory
Transition metal dopants
Hydroxyapatite

ABSTRACT

We present the first comprehensive investigation of transition metal-substituted Hydroxyapatite (TM-HAP) materials for photocatalytic CO_2 reduction (CO_2RR). Density functional theory (DFT) was used to study in a systematic manner the stability of 3d, 4d, 5d transition metal dopants on the HAP ($00\bar{1}1$) surface, analyzing their stability, activity, and selectivity for photocatalytic CO_2RR. DFT results allowed to narrow down the selection to three transition metal elements (Co, Ni, Mo) based on their structural stability, band structure and performance. A selective analysis of product formation for carbon monoxide and formate was made, showing that TM dopants facilitate the initial protonation step in the CO_2 reduction by adsorbing H_2 molecule on TM atoms and then dissociating it into two hydrogen atoms. The performance of Ni- and Co-HAP towards the reaction activity is consistent with experimental results. Mo-HAP stands as a new and attractive photocatalyst for further investigation, given its excellent predicted performance.

1. Introduction

The global economy heavily relies on fossil fuels as a primary energy source for power generation, transportation, and industry, resulting in massive CO_2 and other greenhouse gases emissions that contribute to climate change. Carbon capture, utilization, and storage (CCUS) technologies, aiming to capture, utilize or store CO_2 from industrial processes and power generation before releasing it into the atmosphere [1,2] have been identified by the International Energy Agency as one of the key technologies to decarbonize the society in the short-to-medium term. Among the CO_2 utilization technologies, carbon dioxide reduction reaction (CO_2RR) involves converting CO_2 into value-added products. This can be done by electrochemical processes (using electrical energy for the chemical conversion) or by photocatalytic processes (using semiconductors to absorb photons from light and generate electron-hole pairs for initiating redox reactions). The main advantages of photocatalytic CO_2 conversion versus electrochemical conversion are that it operates at ambient temperatures and pressures (instead of the high-temperature and high-pressure requirements of some electrochemical processes) and photocatalyst can be designed with high efficiency and tuning selectivity, making it a promising approach for converting solar energy into chemical fuels. Meanwhile, about 10% of the solar energy received on 0.3% of the Earth's surface would be enough to fulfill the expected energy needs in 2050, if properly converted [3]. This technology provides an alternative to traditional petrochemical-based production, advancing a sustainable energy future [4–7].

Recently, it has been identified by our research groups and others that hydroxyapatite (HAP, $Ca_{10}(PO_4)_6(OH)_2$), a calcium hydroxyphosphate that constitutes about 70% of bone and teeth mass, can be a promising photocatalyst for CO_2RR when properly doped with metal cations [8,9]. The HAP matrix is a low cost material and presents exceptional properties of water insolubility, thermal and chemical stability, easy preparation at large scale and highly functionalized surface allowing multiple ion substitutions [10,11]. The flexibility of the HAP structure enables functionalization and modulation of the acid-base sites by substituting cations (such as transition metals) for Ca^{2+}, and anions (such as CO_3^{2-}) for hydroxyl (OH^-) or phosphate (PO_4^{3-}) basic sites [12]. Indeed, the hexagonal crystalline structure and amphoteric surface of HAP possesses a specific affinity towards CO_2, even at room temperature [13]. In fact, CO_2RR intermediates can be conveniently stabilized and coordinated on acidic and/or basic sites of HAP surface. However, some

* Corresponding authors.
E-mail addresses: Lourdes.vega@ku.ac.ae (N. López), nlopez@iciq.es (L.F. Vega).

https://doi.org/10.1016/j.jcou.2024.102692
Received 11 November 2023; Received in revised form 21 January 2024; Accepted 24 January 2024
Available online 1 February 2024

other studies have suggested a diverse possible pathway that CO_2 can interact with basic OH^- and O^{2-} of PO_4^{3-} groups to form hydrogenocarbonates (HCO_3 *) and surface $(PO_x)_s$-carbonate species, respectively [14].

The presence of a proper band gap is crucial for photocatalytic applications [15]. Although stoichiometric defect-free HAP is generally considered an insulator material with a reported band gap of around 3.95 eV [16], it has been demonstrated that HAP doping promotes new intra-band states, allowing for a broader range of light absorption [17]. For example, Liu *et al.* [18] reported that Fe-HAP can be synthesized facilely by a low cost ion-exchange method and exhibit promising visible-light photocatalytic activity toward rhodamine B degradation, showing the synthesized Fe-HAP material was quite stable after performing for three times the photocatalytic reaction. It is important to note that the effect of transition metal doping on the band gap depends on various factors, such as the dopant and its concentration, as well as the synthesis procedure. Moreover, HAP exhibits high surface area and excellent stability even after calcination. The combination of cost benefits, eco-friendliness, simple preparation, and reusability are huge advantages of this material for a large scale use [8,19].

Recently, transition metals (TM) have been extensively investigated for CO_2RR [20–23] due to their high activity and selectivity in producing hydrocarbons, alcohols, and other C_3 products. As previously reported, the nature of TMs doped on the HAP surface plays a critical role in determining the catalytic activity and selectivity of the CO_2RR [13,24]. *In situ* Diffuse Reflectance Infrared Fourier Transform Spectroscopy (DRIFTS) measurements proved that surface hydroxyl (*OH) and oxide (*O) of PO_4^{3-} groups from Ni-doped HAP are directly involved in the interaction with chemisorbed CO_2. The Ni^0 single atoms and/or clusters can be responsible for CO formation while the Ni^0 nanoparticles may be responsible for CH_4 formation. Ni-HAP catalyst was also investigated in CO_2 reforming of CH_4 reaction under thermal treatment to enhance the regeneration capacity of the deactivated catalyst [25]. Furthermore, Chong *et al.* [26] reported that HAP/TiO_2 showed about 40 times enhancement in photocatalytic CO_2 reduction with over 95% selectivity towards CH_4 compared to TiO_2. The characterization results showed the Lewis basic sites (*O in PO_4^{3-} groups) enhanced the adsorption/activation of CO_2, and Lewis acidic sites (Ca^{2+}) facilitated the adsorption/dissociation of H_2O, respectively.

Hence, it is worthwhile to investigate doped HAP as a catalytic platform for CO_2RR, and particularly, to explore detailed reaction mechanisms of CO_2RR on HAP-based catalysts from atomistic simulations, as a guide to design ad-hoc photocatalysts for this application. Herein, we have employed density functional theory (DFT), for screening a wide range of transition metal atoms in 3d, 4d, and 5d series (i.e., Sc, Ti, V, Cr, Mn, Fe, Co, Ni, Cu, Zn; Y, Zr, Nb, Mo, Tc, Ru, Rh, Pd, Ag, Cd; Hf, Ta, W, Re, Os, Ir, Pt, Au, Hg), anchored on HAP with a single Ca vacancy for their photocatalytic CO_2RR performance, as shown in Fig. 1. The formation energy of modified HAP surfaces is used to evaluate the thermodynamic stability of the structures. Then electronic structures such as density of states (DOS) and band gap are checked for favorable responses to visible light, high photo-induced electron-hole separation efficiencies, and sufficient potentials for CO_2RR. Moreover, by analyzing the reaction energies and reaction pathways, DFT can provide insights into the factors that affect C_1 product selectivity, Hydrogen Evolution Reaction (HER) competition and guide the design of more efficient photocatalysts for CO_2 reduction.

2. Methodology

Computational screening using simple but thermochemically reasonable descriptors is crucial for efficiently identifying suitable co-catalyst among countless TM doping options for HAP. In this regard, we have developed and applied a screening procedure to determine the most appropriate TM dopants for the HAP, as explained next.

Spin-polarized density functional theory (DFT) calculations were

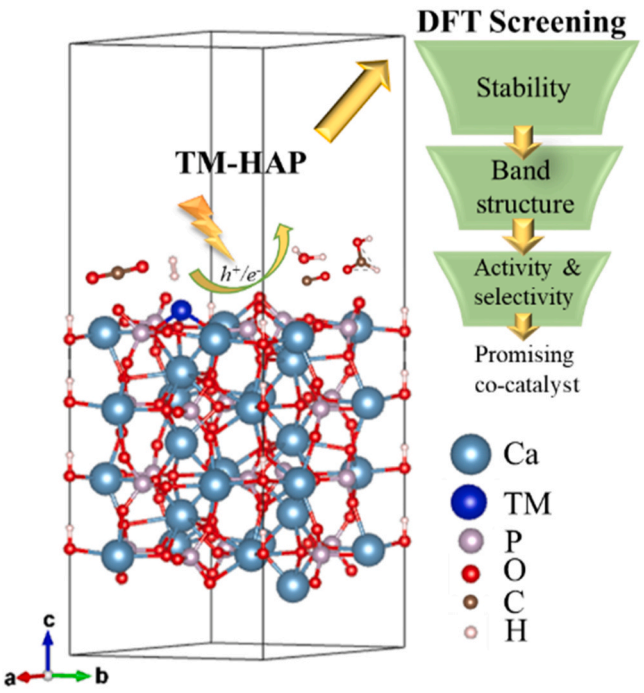

Fig. 1. Side view of an optimized TM-HAP configuration and a schematic of the top-down screening approach (including stability, band structure, activity and selectivity screening) devised to screen promising TM-HAP catalysts for CO_2RR.

carried out using the VASP (Vienna Ab initio Simulation Package, version 6.2.0) software [27]. For structural optimizations, the exchange-correlation interactions between electrons were described by the generalized gradient approximation (GGA) with the Perdew–Burke–Ernzerof (PBE) [28] functional and projector-augmented-wave (PAW) pseudopotentials [29]. However, to account for the underestimation of band gaps by PBE methods, band structures were calculated by using the Heyd-Scuseria-Ernzerhof (HSE06) [30] hybrid functional with the 25% Hartree-Fock exchange. The long-range van der Waals (vdW) interactions were described using DFT-D3 method with no damping [31]. A plane-wave basis set with an energy cutoff of 500 eV was adopted and the electronic self-consistency was converged to within 10^{-5} eV/atom. The ionic positions were optimized until the residual force acting on each ion was below 0.02 eV/Å. The bulk of $1 \times 1 \times 1$ unit cell and slabs of 1×1 unit cell with 7 layers were selected for the calculations. The upper three layers underwent relaxation while the bottom layers were constrained to bulk geometric parameters in order to simulate a bulk environment. Monkhorst-Pack k-point meshes of $3 \times 3 \times 1$ were used for the TM-HAP slab systems, respectively.

To efficiently identifying suitable co-catalyst among countless TM doping options for HAP, we have developed and applied a top-down screening procedure to determine the most appropriate TM dopants for the HAP surface, as shown in Fig. 1. The process began with an examination of the structural stability of different TM-HAP surfaces, assessed through the calculations of binding energies (E_b), cohesive energies (E_c), and formation energies (E_f). Subsequently, band gap was introduced as a secondary descriptor to estimate the optical and electronic properties of each surface, thus enabling the identification of potential candidates for photocatalytic CO_2RR. Finally, the reaction energies and reaction pathways were compared to evaluate catalytic activity and selectivity. Using these criteria, transition metal dopants fulfilling the screening criteria were identified as the most promising co-catalysts for photocatalytic CO_2RR.

The surface energy (γ) is a critical property to be considered with respect to the stability and reactivity of the studied HAP surfaces, which

can be calculated as [32]:

$$\gamma = \frac{E_{TM-HAP} - mE_{bulk}}{2A} \quad (1)$$

where E_{TM-HAP} is the energy of the relaxed slab, E_{bulk} is the energy of bulk HAP per atom, m is the number of atoms in the surface slab, and A is the area of one side of the slab.

Besides, the formation energy is the energy required to form a specific compound or material from its constituent elements in their standard states, which is related to the stability of a material or compound. The formation energy of TM embedded in the defected HAP (ΔE_f) is calculated as follows [33]:

$$\Delta E_f = (E_{TM-HAP} - a.\mu_{Ca} - b.\mu_P - c.\mu_H - d.\mu_O - n\mu_{TM})/(a+b+c+d+n) \quad (2)$$

where E_{TM-HAP} is the same as in Eq. (1), a, b, c, d and n are the number of Ca, P, H, O and TM atoms in the system, respectively, and $\mu$are the chemical potentials from their bulk structure. A more negative value of E_f indicates better thermodynamic stability.

The binding energy is the energy required to remove a single atom or molecule from the surface of a material. It is often used to evaluate the strength of the bond between an atom or molecule and a surface (a more negative value indicates better binding) and predicts the reactivity of the surface towards other atoms or molecules. The binding energy (E_b) of TM atoms embedded in the defected HAP surface is calculated as follows [34]:

$$E_b = E_{TM-HAP} - E_{HAP} - n.E_{TM} \quad (3)$$

where n is the number of transition metal atoms, E_{TM-HAP}, E_{HAP} and E_{TM} denote the total energies of TM embedded HAP surface, defected HAP surface and TM atoms, respectively.

The cohesive energies of bulk metal materials (E_c) can be obtained by [34]:

$$E_c = (E_{bulk} - n.E_{TM})/n \quad (4)$$

where the E_{bulk} is the energy of bulk metal and E_{TM} is the energy of a single metal atom.

The term band gap refers to the energy difference between the highest energy level of the valence band and the lowest energy level of the conduction band in the electronic band structure of a material. The electronic band structure plays a crucial role in determining the electrical and optical properties of materials, including their ability to conduct electricity and their response to light. In CO_2RR, the band structure is studied as a descriptor for the ability of a photocatalyst to generate electron-hole pairs upon light absorption, as well as its activity in initiating CO_2 reduction [35,36]. The band gap of a photocatalyst determines the energy required to excite electrons from the valence band to the conduction band, which initiates electron transfer and drives the photocatalytic reaction [37,38]. Specifically, TM doping can introduce new defect levels or modify the valence band and conduction band, thereby altering the optical and electrical properties of the photocatalyst. When designing and optimizing photocatalysts, the impact of TM doping on the band gap and band edge position should be considered and investigated to achieve the desired catalytic performance, hence, this descriptor is considered as part of the screening process developed in this work.

The potential of the valence band (E_{VB}) and the bottom conduction band (E_{CB}) are fundamental properties of a semiconductor photocatalyst. The E_{CB} and E_{VB} are estimated by [39,40]:

$$E_{CB} = E^e + \chi - \frac{1}{2}E_g \quad (5)$$

$$E_{VB} = E_{CB} + \frac{1}{2}E_g \quad (6)$$

where E^e is the energy of free electrons on the hydrogen scale (E^e =−4.5 eV),χ is the Pearson absolute electronegativity of the semiconductor, and E_g is the bandgap of the semiconductor. For example, for a semiconductor A_aB_b, χ is calculated by:

$$\chi = \left(E_A^a \times E_B^b\right)^{\frac{1}{a+b}} \quad (7)$$

where E_A^a and E_B^b are the absolute electronegativity values of A and B, respectively. The letters a and b indicating the stoichiometry of each element A and B in the semiconductor A_aB_b, respectively.

For the reactions involving the reduction of CO_2 to formate and CO, the reaction energy (ΔE_{rec}) are defined as [41]:

$$\Delta E_{rec} = E_{FS} - E_R \quad (8)$$

where E_{FS}, and E_R are the total energies of the final state and the reactant in each elementary reaction, respectively. A negative value of reaction energy corresponds to an exothermic reaction.

Furthermore, to investigate the competitive selectivity of generating hydrogen gas for CO_2RR progress, the Gibbs free energy for HER needs to be analyzed and calculated as:

$$\Delta G_H = \Delta E_H + \Delta E_{ZPE} - T\Delta S \quad (9)$$

where ΔE_H represents the adsorption energy of intermediates H for HER (unfavorable site reaction of CO_2RR), T denotes the temperature (set as 300 K), ΔE_{ZPE} and ΔS are the difference in zero-point energy (ZPE) and the entropy between the adsorbates adsorbed state and gas phase, respectively. Specifically, the adsorption energy of H adsorbate is defined as:

$$\Delta E_H = E_{TM-HAP+H} - E_{TM-HAP} - 1/2E_{H_2} \quad (10)$$

where $E_{TM-HAP+H}$ denotes the energy of TM-HAP with adsorbed hydrogen atoms H* , and the E_{H_2} is the energy of H_2 in the gas phase.

Additionally, the desorption ability of CO products on the surface, can be obtained from their adsorption energy ΔE_{ad} as:

$$\Delta E_{ad} = E_{TM-HAP+CO} - E_{TM-HAP} - E_{CO} \quad (11)$$

where $E_{TM-HAP+CO}$ denotes the energy of TM-HAP with adsorbed CO* molecules, and the E_{CO} is the energy of CO in the gas phase.

3. Results and discussion

Understanding the surface morphology of HAP crystals is essential for developing new materials with enhanced catalytic properties [42]. In this context, we first investigated different structural terminations of HAP crystals to find out the most stable surfaces. To achieve this goal, we employed DFT calculations to calculate the surface energies (see Eq. 1) of three low-index surfaces of HAP which has been reported in literature [43,44], including $(10\bar{1}0)$, $(01\bar{1}0)$, $(00\bar{0}1)$ with (1 × 1) supercell size (shown in Fig. S1 in the SI). With the increase of surface energy, the surface stability decreases [45]. Our results showed that among the different terminations considered, the $(00\bar{0}1)$ surface was the most stable (surface energy of 0.124 eV/Å^2), followed by the $(10\bar{1}0)$ and $(01\bar{1}0)$ surfaces, with surface energies of 0.181 and 0.182 eV/Å^2, respectively. It is observed that the surface energy of the $(00\bar{0}1)$ surface is significantly lower than that of the other surfaces, indicating that this facet would be the most energetically favorable one to expose under ambient conditions [46]. The high stability of this surface can be attributed to the strong covalent bonding of PO_4-Ca-PO_4 within each layer and the relatively weaker van der Waals interactions between layers, which creates a delicate balance between the intra-layer and inter-layer interactions and results in a mutually constrained structure within the surface layers. Additionally, the exposed surface ions of the (001) facet have the lowest coordination numbers compared to other

facets, which further stabilizes this surface by reducing the energy required to break surface bonds. By focusing on the most stable HAP surfaces, one can gain a better understanding of how dopants may interact with the HAP crystal, and how this interaction can be leveraged to achieve desired electronic properties and catalytic performance. This knowledge can be utilized to guide future studies on the substitution of transition metal into the HAP structure.

3.1. Structural stability of the TM-HAP

Analyzing the dopant-host interaction through calculations of formation energy, binding energy, and cohesive energy, as well as investigating the dopant's proximity to neighboring atoms, can provide valuable insights into the doping sites and configurations, guiding the selection of promising co-catalysts for further screening. Hence, a thorough investigation of the structural stability of TM dopants on HAP was conducted by DFT to ensure adequate structural and chemical stability.

Fig. 2 and Fig. S2 in the SI illustrate the formation energies (E_f, Eq. 2) of TM-HAP and binding energies (E_b, Eq. 3) of TM atoms bonded with the HAP surface, respectively. A negative E_f indicates that the synthesis process of TM-HAP is exothermic and thermodynamically favorable. Based on the results in Fig. 2, all the E_f of TM-HAP are negative, from − 3.10 eV (Y-HAP) to − 3.00 eV (Os-HAP). Certain trends in the values can be observed based on the location of the dopant element in the periodic table. Generally, the formation energies and binding energies of the dopants become less negative as the dopant moves from 3d to 5d elements. This trend can be explained by the fact that moving from 3d to 5d elements, the atomic radius of the elements increases, while the effective nuclear charge experienced by the valence electrons remains nearly constant. As a result, the valence electrons in the 5d elements are less strongly attracted to the nucleus and are more easily removed or perturbed from their positions in the lattice, resulting in less stable dopants. However, the trend of the formation energy is not continuously less negative across all 4d, and 5d elements, especially Os-HAP shows the most positive E_f, revealing a potential difficulty to find an experimentally synthesis route for this catalyst. It is also observed that materials incorporating 5d elements generally exhibit lower stability compared to those with 3d and 4d metals. This distinction in stability can be attributed to the shielding effect which diminishes the effective nuclear charge. The outer shell electrons in 5d elements have reduced effective nuclear charges with less tightly bound, leading to increased instability in these TM-doped HAP materials. And there are several factors that can contribute to the volcano trends for 4d and 5d elements, where E_f increases rapidly from group 3 to 8 (Y to Ru in 4d and Hf to Os in 5d). For example, the oxidation state of Yttrium typically shows a + 3 state, whereas Mo can exhibit multiple oxidation states (from +2 to +6), which can lead to instability in the doped materials as the dopant atoms can easily change their oxidation state, disrupting the electronic balance within the host lattice. Also, the larger atomic size can cause a greater lattice distortion when these atoms are introduced into the host material, leading to structural instability. In the case of 10 to 12 columns elements, especially Zn, Cd, Hg, the *d*-orbital is full with ten electrons and shield the electrons present in the higher *s*-orbital, resulting in increasing stability and more negative formation energy [47]. Additionally, the half-filled *d*-orbital elements, such as Os and Ir, have high electron affinity and electronegativity in their + 2 oxidation state, which results in a higher formation energy and less likely to substitute for Ca^{2+} in the lattice. Moreover, a smaller metallic radius of the dopant ion relative to the host ion may lead to a lower stability due to the larger lattice strain and charge transfer. Conversely, a larger metallic radius may enhance the compatibility and homogeneity of the dopant in the host lattice, as well as the dispersion and accessibility of the active sites.

Moreover, if the binding energy of a dopant is more negative than its corresponding cohesive energy value as shown in Fig. 2, it suggests that the dopant atoms are energetically favorable at the doping site and are

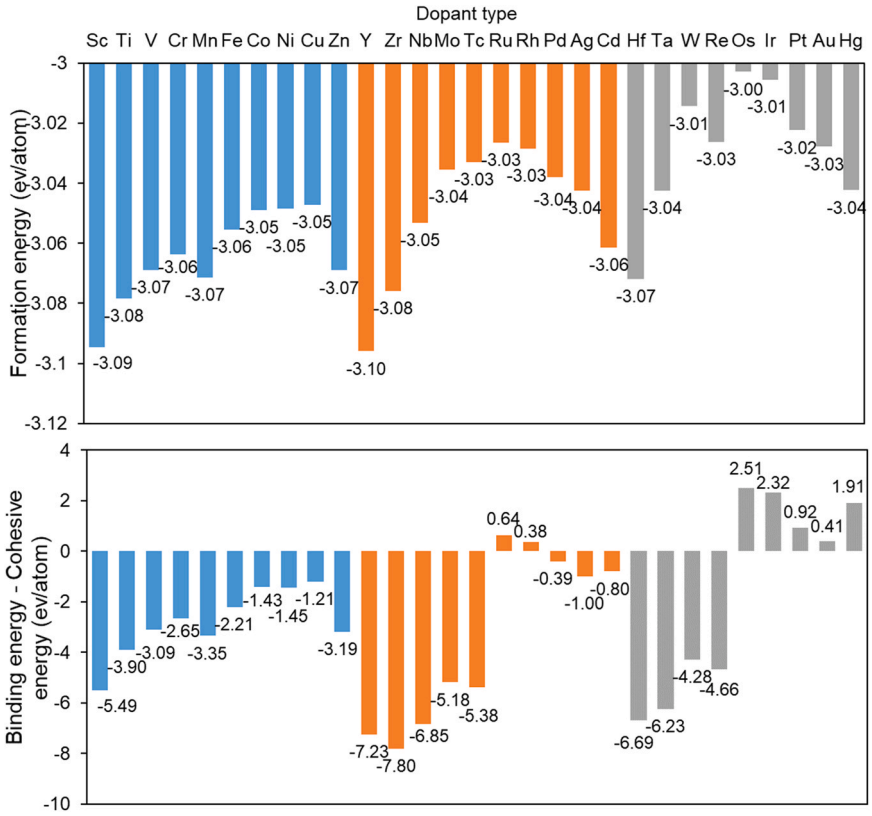

Fig. 2. (top) The formation energy E_f (upper) of TM-HAP catalyst, and (bottom) the binding energy E_b of TM embedded into HAP surface minus the cohesive energy of TM bulk (down). The order of the TM dopant from left to right is 3d series (blue), 4d series (orange) and 5d series (grey).

likely to remain there under typical reaction conditions [48,49]. While a more positive E_b compared to E_c implies a higher probability of transition metal aggregation and the formation of clusters on the support surface [50]. These metal clusters could potentially obstruct the formation of active sites, leading to a reduction in catalytic efficiency. As we can see from Fig. 2, it is apparent that 7 TM (Ru, Rh, Os, Ir, Pt, Au, and Hg) have their binding energy greater than cohesive energy (i.e., positive values), which contradicts the requirement for stable and uniform doping on the surface to act as active sites. This could be attributed to the inherent properties of the later TMs in 4d and 5d. These metals have high electron affinity and electronegativity with relatively large atomic radii and limited *d*-orbital vacancies, which make them having a higher tendency to cluster and agglomerate on the surface. Furthermore, as inferred from Fig. S3 in the SI, where the bond length between TM atom and the closest oxygen atom from the TM-HAP surface is depicted, the later transition metals of the 4d and 5d series generally exhibit longer bond lengths in the TM-HAP system, which is consistent with the trend of atomic radii for transition metal elements, where smaller atomic radii usually correspond to shorter bond lengths. Moreover, this observation is in line with the trend of binding energy, as transition metal elements that exhibit shorter bond lengths and also tend to have higher binding energy.

Overall, these 7 metals (Ru, Rh, Os, Ir, Pt, Au, and Hg) were found to be relatively unstable and unsuitable for doping on the HAP surface, as their binding energies exceed their cohesive energies. Hence, these metals are excluded from further consideration, and we will focus on exploring the band structure properties of the remaining potential metal dopants.

3.2. Band structure of the TM-HAP

Since the standard Gibbs free energy of CO_2 formation is − 4.088 eV, a significant amount of energy is needed to convert it into value-added products. Efficient separation and transfer of the photogenerated charge carriers to the particular catalytic active sites of the photocatalysts triggers the redox reaction, resulting in chemical fuel [51]. Table S1 in the SI shows a list of the standard reduction potentials (at 1 bar, 25 °C, pH=0) for CO and HCOOH that involves the transfer of two electrons [52]. For photocatalytic reduction of CO_2 in the presence of water, the CB must be negatively paralleled to the reduction potential of CO_2 reduction to CO (−0.105 V vs. normal hydrogen electrode (NHE)) and CO_2 reduction to HCOOH (−0.169 V vs. NHE) at pH = 0. In the case of photo-assisted CO_2 reduction using TM doped-HAP, the reduction of CO_2 is facilitated by the presence of H_2. Whereas the top of the VB should be positioned more positively than the oxidation potential of H_2 (0 V vs. NHE at pH 0). Additionally, the band gap width of semiconductors should be less than 3.0 eV (>400 nm) and greater than 1.23 eV (<1000 nm) to be utilized in the UV/visible region (i.e., wavelengths from ca. 380 to 750 nanometers).

Therefore, the calculated bandgap and band edge position of TM-HAP were compared with pristine HAP surface and results are presented in Fig. S4 in the SI and Fig. 3, respectively. It is observed that most of TM dopants generate impurity states near the Fermi level and reduce the band gap of the catalyst, leading to improved absorption of visible light, electron transfer and photocatalytic activity. However, doping with Mn and Fe results in an increased band gap, so it requires higher energy photons to be excited and reduces absorption ability towards visible light. As inferred from Fig. 3, the valence band edge (blue line in the figure) is more positive than the oxidation potential of H_2/H^+, and the conduction band edge of pristine HAP surface has a lower energy potential compared to the reduction potential of CO_2/COOH or CO_2/CO. However, the band gap of HAP is larger than 3 eV, which indicates that CO_2RR cannot occur under visible light at the pristine HAP surface. Most of the TM dopants have a very narrow band gap (e.g., Sc, Cu, Y, Zr, Ag and Hf), which means it is very easy to excite an electron from the ground state into an excited state under light irradiation. However, these extremely small energy gap prevents them from straddling the reduction potential conditions for CO_2RR. Only Co, Ni, Mo, and Tc dopants, as highlighted in Fig. 3, exhibit suitable band gap and positions of CB and VB for utilization in the CO_2RR process. Furthermore, these TM dopants lower the reduction potential compared to pristine: electrons can transfer from HAP to TM dopants, then creating an electron reservoir to effectively trap electrons from the CB of HAP, which promotes electron extraction and slows the recombination of electron-hole pairs. Finally, Zn doping does not significantly narrow the band gap as well.

The Partial Density of States (PDOS) were calculated to gain a comprehensive understanding of how Zn, Mn and Fe dopants impact the band gap of HAP. It can be clearly observed in Fig. 4 that the Zn doping in HAP does not cause the formation of new energy levels within the forbidden gap, with the most prominent peaks observed in the energy range of − 6 to − 10 eV. This explains why there is no notable reduction in the band gap of HAP with Zn doping. Similarly, the DOS analysis in Fig. 4 indicates that Mn and Fe doping in HAP do not enhanced impurity states within the forbidden band, meanwhile, they slightly shift the energies of the valence band and conduction band, leading to an increase in the band gap.

We further applied PDOS analysis (see Fig. 5) on the four best potential candidates, Co, Ni, Mo, and Tc, and compared them with the pristine HAP surface to reveal the distribution changes of electron density at different energy levels. The asymmetric distribution of

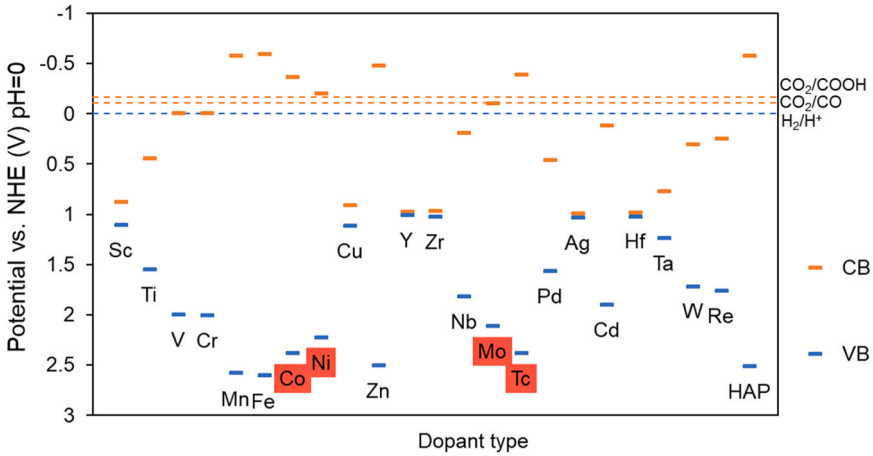

Fig. 3. Relationship between band structure of TM-HAP semiconductor and redox potentials of CO_2 and H_2O computed with the HSE06 hybrid functional. The order of the TM dopant from left to right is 3d series to 5d series. Highlighted metals are suitable for further use in a photocatalytic CO_2RR process.

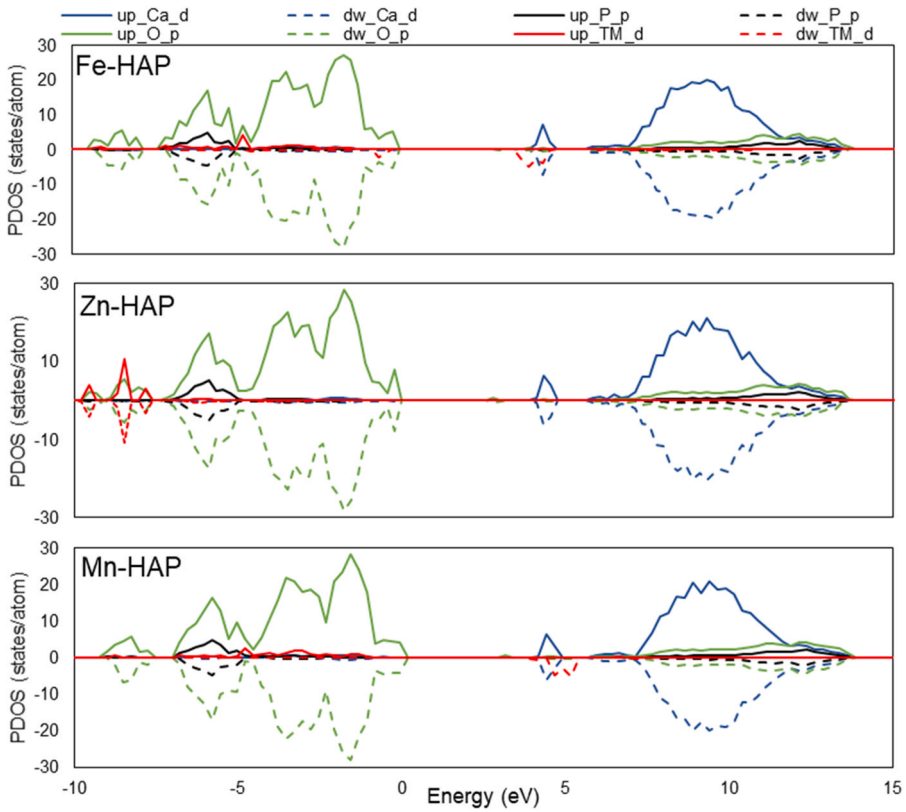

Fig. 4. Partial density of state (PDOS) of selected TM-HAP surface from DFT calculations. The upward electron spin is denoted as up, downward spin is denoted as dw, p represents the sum of p orbital, d represents the sum of d orbital. The Fermi level is set to 0.

electron density in spin-up and spin-down electronic states in TM-HAP indicates the presence of spin polarization, which refers to the presence of unpaired electrons with different spin orientations in the material. In addition, PDOS of TM-HAP reveals a substantial occupancy of spin-down or spin-up for TM *d*-orbitals (with high density of states) in the energy range of 2–4 eV. This suggests that TM dopants create a higher concentration of electrons near the Fermi energy and an activation energy region to faster the electron migration. Furthermore, in the energy range of − 1–0 eV, the *p*-orbitals of oxygen atoms exhibit shifts in energy levels and changes in peak intensities, which indicates the existing of electron transfer between the oxygen atoms and results in the formation of ionic or metallic bonds. Based on the electronegativity values of these elements, Mo has the highest electronegativity, as reflected by higher peak intensities near fermi energy in the PDOS. Conversely, Co has the lowest electronegativity, as reflected by lower PDOS peak intensities at lower energy levels.

Overall, the presence of Co, Ni, Mo, and Tc dopants in HAP material facilitates the migration of electrons, resulting in a narrower band gap with proper band edge position and enhanced electron transport. Hence, in the following sections we present and discuss results concerning their catalytic activity and selectivity towards CO, HCOOH, and their reduction intermediates.

3.3. CO and HCOOH formation and selectivity

The photocatalytic conversion of CO_2 $^{*-}$ species has been proposed to occur through two possible pathways in the literature [53,54]. The first pathway involves the carbon atom in CO_2 $^{*-}$ binding with a hydrogen atom and followed by accepting an electron to form HCOO* (or COOH*). The second pathway involves a hydrogen atom attacking one oxygen atom in CO_2 $^{*-}$ to form a carboxyl radical (*COOH), followed by accepting an electron to form adsorbed carbon monoxide (CO*). CO is a valuable precursor for the further synthesis of various chemicals, such as methanol, acetic acid, and higher hydrocarbons, such as CH_2O or CH_3OH, or the adsorbed CH_4 [55,56]. Formic acid (HCOOH) has also gained significant attention as a renewable energy carrier due to its potential use as a high-density liquid hydrogen storage medium or as a source of hydrogen for fuel cells [57,58]. The corresponding pathways of CO and HCOOH production are as follows:

$$CO_2 + * \rightarrow CO_2* \quad (12)$$

$$CO_2* + H^+ + e^- \rightarrow COOH* \text{ or } CO_2* + H^+ + e^- \rightarrow HCOO* \quad (13)$$

$$COOH* + H^+ + e^- \rightarrow CO* + H_2O \text{ or } HCOO* + H^+ + e^- \rightarrow HCOOH* \quad (14)$$

$$CO* \rightarrow CO + * \text{ or } HCOOH* \rightarrow HCOOH + * \quad (15)$$

where the asterisk (*) denotes that the species is in an intermediate state or adsorbed on a surface.

Therefore, understanding the formation and selectivity of carbon monoxide and formic acid is crucial for elucidating the mechanisms of CO_2RR because these are important building blocks for the production of value-added chemicals and fuels from CO_2 [59–61]. Fig. 6 illustrates the distinct reaction pathways and reaction energies for the generation of CO and HCOOH, the corresponding structures are shown in Table 1. The selectivity of CO formation over HCOOH formation among these 4 TM dopants (Co, Ni, Mo, and Tc) can be deduced from the changes in the reaction energy. The positive reaction energies for HCOOH formation indicate that generating HCOOH is thermodynamically unfavorable and endothermic, compared to CO formation. This could be due to the nature of the dopant atoms and their interactions with the CO_2 molecule, which may favor the formation of CO over HCOOH. But the selectivity and energy change trends in the formation of CO and HCOOH may vary depending on factors such as reaction conditions, and chemical environment. Further research and in-depth analysis are needed to fully understand the specific reaction mechanisms and energy changes under different experimental conditions and catalyst properties.

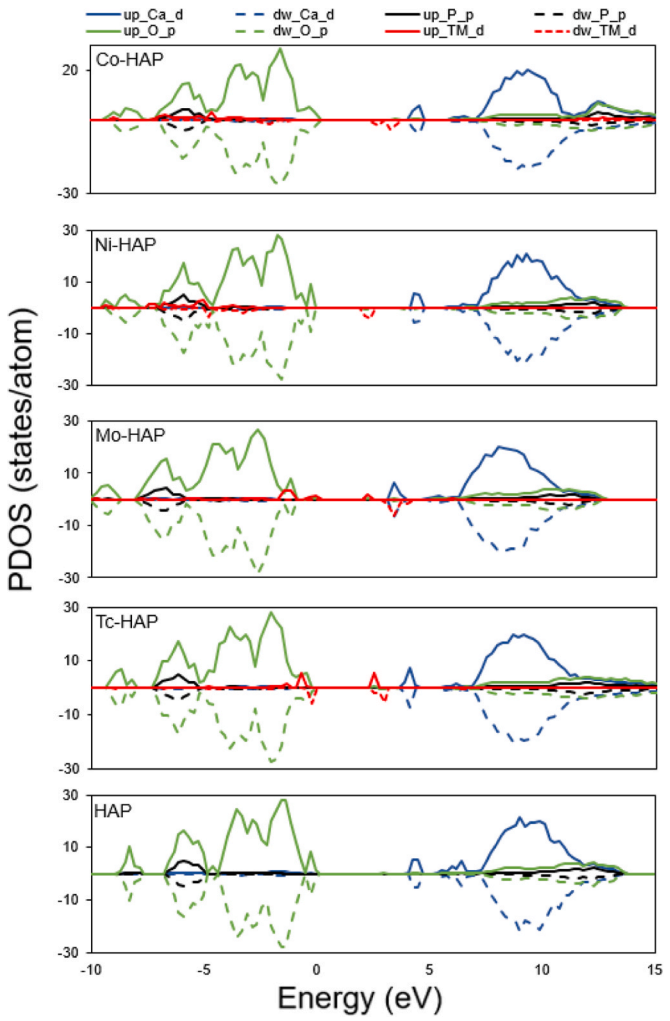

Fig. 5. Partial density of state (PDOS) of selected TM-HAP surface from DFT calculations. The upward electron spin is denoted as up, downward spin is denoted as dw, p represents the sum of p orbital, d represents the sum of d orbital. The Fermi level is set to 0.

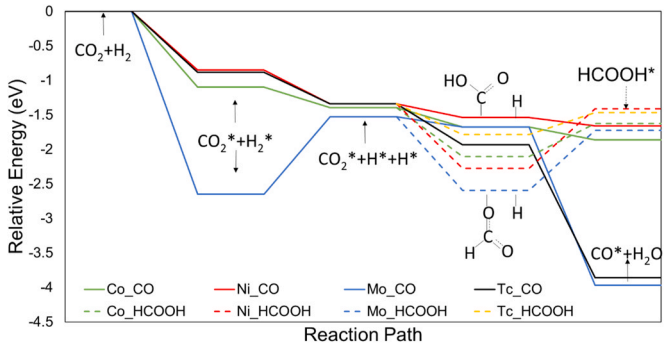

Fig. 6. Proposed mechanism and reaction pathways for carbon dioxide reduction to C_1 products (formate, carbon monoxide). The solid line represents the reaction pathway for CO, while the dashed line represents the reaction pathway for HCOOH.

Comparing the reaction energies of generating CO in Fig. 6, it appears that Mo and Tc dopants may be more effective in facilitating the exothermic reduction of CO_2 to CO compared to Co and Ni dopants, as they exhibit more negative reaction energies and lower energy barriers, which typically correlate with higher catalytic activity. As presented in Table 1, the Mo catalyst has a significant role in cleaving the CO_2 bond to form CO molecules. The formation of CO already starts during the adsorption step of CO_2 without requiring additional dissociation steps, which may imply that Mo catalyst exhibits higher catalytic activity and selectivity in CO_2 reduction reactions. The adsorption of CO on the Mo-HAP surface with a bond length of 1.83 Å is significantly shorter than other surfaces, and according to the adsorption energy data in Table S3 in the SI, it can be observed that the adsorption energies of CO on Mo and Co doped HAP are relatively higher than other systems with a value of − 1.84 eV and − 1.64 eV, respectively. It suggests that the adsorption of CO on the Mo-HAP surface is relatively stronger, restricting the desorption of CO from the surface. For photocatalytic reactions, desorption can potentially affect the catalytic efficiency of the photocatalyst because the reactant molecules or intermediates leaving the surface may be re-excited by photons and re-adsorbed onto the catalyst surface, which can affect the reaction rate. Thus, while Mo and Tc exhibit strong selectivity towards CO, their difficulty in desorption may hinder their catalytic efficiency.

According to the structural data in Table 1, it is worth noting that the elongation of the H-H bond length from 0.737 Å (the bond length for isolated molecular hydrogen) to 0.80 Å when H_2 adsorbs onto the TM site indicates that there is weakening of the H-H bond upon adsorption. This suggests that the TM site plays an important role in weakening the H-H bond and providing protons for subsequent reactions. Moreover, when COOH* adsorbs on the surfaces of these TM-HAP catalysts, the bond length between C and TM is always shorter than the bond length between O and TM, indicating that COOH* primarily adsorbs on the TM-HAP surface through the C atom, which may enhance the selectivity towards CO production. These favorable surface properties and structures of TM-HAP catalysts are beneficial for their higher catalytic activity and selectivity in promoting CO formation in CO_2 reduction reactions.

Based on the limited reports available in the literature about the effect of phosphate groups on CO_2 reduction mechanisms [10,13], it is plausible to assume that TM atoms promote the formation of H* species as H_2 molecule tends to preferentially adsorb and dissociate into two hydrogen atoms on TMs, providing a proton to gaseous CO_2 that has chemisorbed with HAP surface or TM atoms. The CO_2 molecule chemisorbed on the surface further react with the decomposed H atoms to produce HCOO* and COOH* , thereby this first proton transfer process will facilitate the formation of intermediate species in the subsequent steps of the reaction [13].

Apart from the catalytic activity and selectivity, the hydrogen evolution reaction (HER) -an unwanted side reaction- should be considered [62,63]. Reduction of protons to form hydrogen gas ($2\,H^+ + 2e^- \rightarrow H_2$) is a competing process for the reduction of CO_2 * (CO_2RR) (Eqs. 13 and 14). According to the Sabatier principle [64], the active site with a ΔG_H closest to zero demonstrates the best H_2 evolution performance in electrocatalysis applications, and this is also applicable to the photocatalytic H_2 evolution [65]. Although there are some contradictions in the literature, however, there is still a strong consensus that the active hydrogens have ΔG_H closest to zero. Because a higher positive value of ΔG_H indicates a stronger resistance for the reactant adsorption and chemical reduction reaction; conversely, a more negative value of ΔG_H denotes that detaching protons or desorption H_2 gas from the catalyst surface will become more difficult. A lower $|\Delta G_H|$) allows for efficient adsorption and release of hydrogen gas at an appropriate level. In Fig. 7, it is shown that the optimal adsorption site is the Tc atom with the HER free energy of − 0.14 eV (close to zero), indicating that the HER side reaction is easy. However, the HER side reaction can be suppressed by adjusting CO_2 partial pressure and the proton concentration [55]. Overall, considering the competitive selectivity of the HER, we narrowed our search for dopants down to 3 TMs (Mo, Ni, Co) from the initial set of 29 TMs, which are expected to improve the photocatalytic performance of HAP and increase the production of CO.

In Fig. S5, we compared the calculated energy profile for CO_2

Table 1
The side view of the most stable configurations for species adsorption on TM-HAP after geometry optimization. Color scheme is the same as in Fig. 1. The distances (Å) marked on the diagram indicate the distances between the adsorbed molecules and the nearest neighbor atoms on the surface.

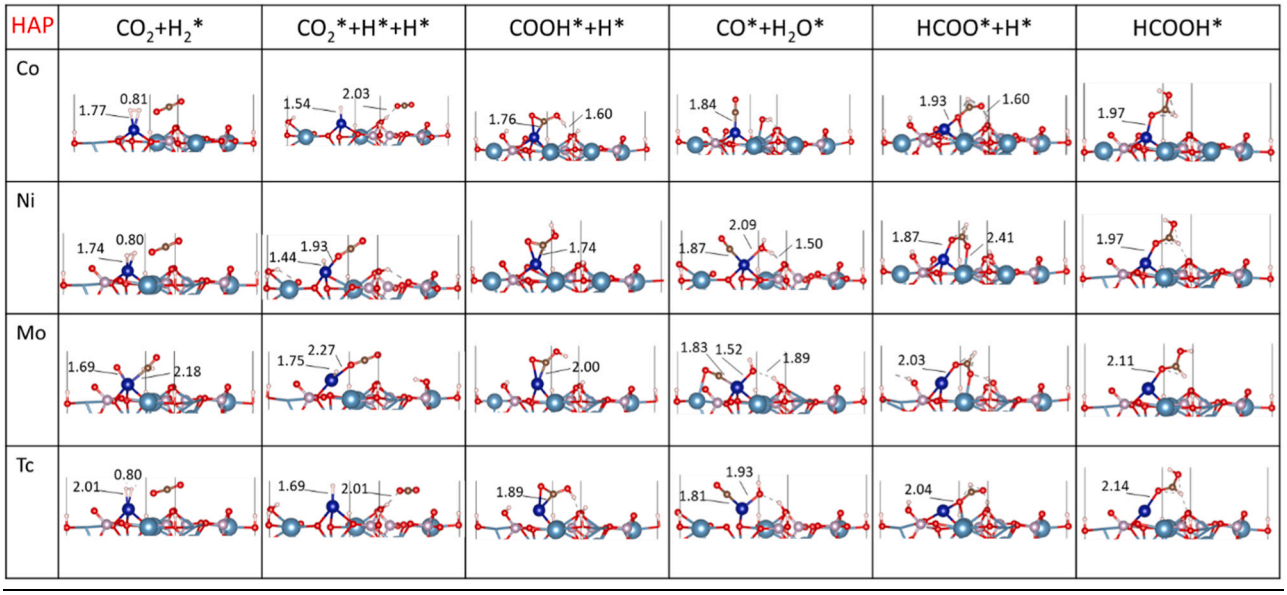

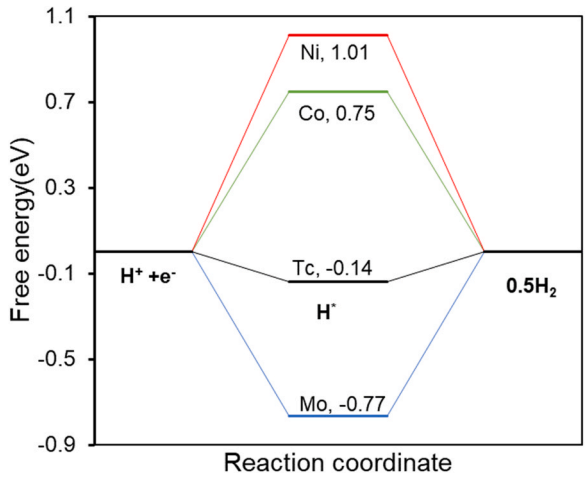

Fig. 7. Energy profile for the HER on the 4 selected TM-doped HAP.

reduction to CO in this work, with published studies in the literature including different catalysts. From the reaction energy changes, it can be observed that the proposed catalysts of this work exhibited relatively high selectivity towards CO. This may be attributed to the presence of Lewis basic and acidic sites on the TM-HAP surface, which can facilitate the adsorption and activation of CO_2 and H_2O, respectively. To further validate these findings, we searched for available experimental studies of HAP doped with Mo, Ni, and Co for CO_2RR applications. It was found that Ni-doped HAP catalysts have been studied for thermal CO_2RR since nickel-based catalysts has high CH_4 selectivity and lower cost as compared to noble metal such as Ru and Rh [13]. In addition, Boukhan *et al.* [66] reported that Ni^{2+} ions exchanged with Ca^{2+} ions of HAP framework at nickel loadings below 1 wt% Ni, validating the rationality of the proposed DFT structure to be synthesized experimentally. The observed activity was close to the thermodynamic equilibrium (78%), which was attributed to the aptitude to chemisorb CO_2 on phosphate (PO_4^{3-}) site from FTIR spectroscopy, as well as the catalytic features of the supported nickel. Similarly, we recently synthesized a series of Co-doped HAP catalysts [8] and found that at low Co loading, Ca cations in HAP are partially substituted, while higher loadings result in the precipitation of small Co nanoparticles on the HAP surface. The CO production rate increased exponentially with temperature; the 15 mol% Co/Ca catalyst exhibited a highest CO production rate of 62 $mmol \cdot g^{-1} \cdot h^{-1}$ under sun illumination and at 400°C for 90 h, the material maintaining its stability for 90 h operation under continuous flow. Operando Raman measurements and DFT results show that H_2 preferentially adsorbs to metallic Co, while CO_2 adsorbs to the HAP surface oxygen. Therefore, the DFT calculations presented in this work are in good agreement with these experimental findings, validating the approach. Notably, Mo-doped HAP has not been specifically studied in the literature for photocatalytic CO_2RR application, and hence a direct comparison is not possible. However, it has been used for other applications. For instance, Thrane *et al.* [67] have investigated the use of MoO_3 (5 to 20 wt%) supported on HAP as catalysts for selective oxidation of methanol to formaldehyde. Compared to the industrial iron molybdate catalyst, the HAP supported MoO_3 exhibited higher activity and selectivity with slower deactivation rate. Moreover, reducible oxides such as cerium oxide (CeO_2) [68,69] and titanium oxide (TiO_2) [70,71] are active catalyst support for photocatalytic CO_2RR. However, the price of TiO_2 is around the range of $6.5 - $15 per kg, while the price range for CeO_2 is around $2.00 - $8.00 per kg. In comparison, the cost of producing modified HAP in industrial quantities can be as low as $1 per kilogram, making it a highly cost-effective alternative [9]. Hence, using HAP as a great alternative, cheap and sustainable support for photocatalytic applications.

4. Conclusions

DFT calculations were used to investigate the structural stability and electronic properties of TM-doped catalysts for CO_2 reduction, as a screening procedure to search for optimal and low-cost materials for photocatalytic CO_2RR process. A total of 29 TM dopants, from 3d to 5d series, were initially selected for the screening. Based on the stability criteria, 7 elements (i.e., Ru, Rh, Os, Ir, Pt, Au, and Hg) were identified to be difficult to uniformly embedded TMs into the HAP surface as active sites and were left out for further screening. Furthermore, we analyzed the electronic structures of the TM-doped systems and identified the changes in the electronic properties of HAP induced by the dopant elements. With respect to the order of TM dopant from 3d to 5d series, the

TM dopants significantly reduce the electronic structure of the surface, which indicates that it is much easier to excite an electron from the bound state into a free state. From these electronic properties, we identified Co, Ni, Mo, and Tc dopants as promising photocatalysts for CO_2 reduction. To study the selectivity and activity of these 4 elements, DFT calculations were performed to explore the energy profiles and reaction pathways for CO_2 reduction. Results indicate that these elements have distinctive reaction mechanisms and products' selectivity for carbon monoxide and formic acid. Among these four transition metals, it was found that Tc is not suitable for the CO_2RR process due to its strong HER competitiveness during the reaction. Hence, the systematic screening procedure highlights Co, Ni and Mo dopants as excellent TM-HAP photocatalysts to be experimentally explored for the conversion CO_2.

CRediT authorship contribution statement

Li yuting: Conceptualization, Data curation, Formal analysis, Methodology, Visualization, Writing – original draft. **Bahamon Daniel:** Conceptualization, Methodology, Software, Supervision, Writing – review & editing. **Vega Lourdes F.:** Conceptualization, Funding acquisition, Project administration, Resources, Supervision, Writing – review & editing. **Albero Josep:** Formal analysis, Validation, Writing – review & editing. **Lopez Nuria:** Conceptualization, Funding acquisition, Methodology, Resources, Supervision, Writing – review & editing.

Declaration of Competing Interest

The authors declare that they have no known competing financial interests or personal relationships that could have appeared to influence the work reported in this paper.

Data availability

Data will be made available on request.

Acknowledgments

We acknowledge the financial support of Khalifa University of Science and Technology, under project RC2–2019-007 (Research and Innovation Center on CO_2 and Hydrogen, RICH Center). Yuting Li acknowledges a grant from China Scholarship Council (CSC), which has sponsored the author's PhD study at Khalifa University, as well as an additional travel grant from Khalifa University to support a research stay at ICIQ, where part of this work was performed. Computational resources from the RICH center and the Almesbar HPC at Khalifa University are gratefully acknowledged. We thank P. Nikacevic for providing the initial HAP structures. J.A. thanks the Spanish Ministry of Science and Innovation for the Ramon y Cajal research associate contract (RYC2021–031006-I financed support by MCIN/AEI/10.13039/501100011033 and by European Union/NextGenerationEU/PRTR) and the financial support (PID2022-141099OA-I00 funded by MCIN/AEI/10.13039/501100011033 and FEDER "Una manera de hacer Europa".

Appendix A. Supporting information

Supplementary data associated with this article can be found in the online version at doi:10.1016/j.jcou.2024.102692.

References

[1] M.A. Sabri, S. Al Jitan, D. Bahamon, L.F. Vega, G. Palmisano, Current and future perspectives on catalytic-based integrated carbon capture and utilization, Sci. Total Environ. 790 (2021) 148081, https://doi.org/10.1016/j.scitotenv.2021.148081.

[2] S. Kar, A. Goeppert, G.K.S. Prakash, Integrated CO_2 capture and conversion to formate and methanol: connecting two threads, Acc. Chem. Res. 52 (2019) 2892–2903, https://doi.org/10.1021/acs.accounts.9b00324.

[3] J. He, C. Janáky, Recent advances in solar-driven carbon dioxide conversion: expectations versus reality, ACS Energy Lett. 5 (2020) 1996–2014, https://doi.org/10.1021/acsenergylett.0c00645.

[4] F. Dattila, R.R. Seemakurthi, Y. Zhou, N. López, Modeling operando electrochemical CO2reduction, Chem. Rev. 122 (2022) 11085–11130, https://doi.org/10.1021/acs.chemrev.1c00690.

[5] A. Wagner, C.D. Sahm, E. Reisner, Towards molecular understanding of local chemical environment effects in electro- and photocatalytic CO_2 reduction, Nat. Catal. 3 (2020) 775–786, https://doi.org/10.1038/s41929-020-00512-x.

[6] H. Lu, Z. Wang, L. Wang, Photocatalytic and photoelectrochemical carbon dioxide reductions toward value-added multicarbon products, ACS ES T Eng. 2 (2022) 975–988, https://doi.org/10.1021/acsestengg.1c00336.

[7] H. Jiang, K. ichi Katsumata, J. Hong, A. Yamaguchi, K. Nakata, C. Terashima, N. Matsushita, M. Miyauchi, A. Fujishima, Photocatalytic reduction of CO_2 on Cu2O-loaded Zn-Cr layered double hydroxides, Appl. Catal. B Environ. 224 (2018) 783–790, https://doi.org/10.1016/j.apcatb.2017.11.011.

[8] Y. Peng, H. Szalad, P. Nikacevic, G. Gorni, S. Goberna, L. Simonelli, J. Albero, N. López, H. García, Co-doped hydroxyapatite as photothermal catalyst for selective CO_2 hydrogenation, Appl. Catal. B Environ. 333 (2023) 122790, https://doi.org/10.1016/j.apcatb.2023.122790.

[9] J. Guo, P.N. Duchesne, L. Wang, R. Song, M. Xia, U. Ulmer, W. Sun, Y. Dong, J.Y. Y. Loh, N.P. Kherani, J. Du, B. Zhu, W. Huang, S. Zhang, G.A. Ozin, High-performance, scalable, and low-cost copper hydroxyapatite for photothermal CO_2 reduction, ACS Catal. 10 (2020) 13668–13681, https://doi.org/10.1021/acscatal.0c03806.

[10] M. Ferri, L. Delafontaine, S. Guo, T. Asset, P. Cristiani, S. Campisi, A. Gervasini, P. Atanassov, Steering Cu-based CO2RR electrocatalysts' selectivity: effect of hydroxyapatite acid/base moieties in promoting formate production, ACS Energy Lett. 7 (2022) 2304–2310, https://doi.org/10.1021/acsenergylett.2c01144.

[11] R.L.P. Rocha, L.M.C. Honorio, E.C. Silva-Filho, J.A. Osajima, R.L.P. Rocha, R.D.D. S. Bezerra, R.L.P. Rocha, P. Trigueiro, T.M. Duarte, M.G. Fonseca, Light-activated hydroxyapatite photocatalysts: new environmentally-friendly materials to mitigate pollutants, Minerals 12 (2022) 1–27, https://doi.org/10.3390/min12050525.

[12] M. Ferri, S. Campisi, M. Scavini, C. Evangelisti, P. Carniti, A. Gervasini, In-depth study of the mechanism of heavy metal trapping on the surface of hydroxyapatite, Appl. Surf. Sci. 475 (2019) 397–409, https://doi.org/10.1016/j.apsusc.2018.12.264.

[13] M.H. Wai, J. Ashok, N. Dewangan, S. Das, S. Xi, A. Borgna, S. Kawi, Influence of surface formate species on methane selectivity for carbon dioxide methanation over nickel hydroxyapatite catalyst, ChemCatChem 12 (2020) 6410–6419, https://doi.org/10.1002/cctc.202001300.

[14] S. Diallo-Garcia, M.Ben Osman, J.M. Krafft, S. Casale, C. Thomas, J. Kubo, G. Costentin, Identification of surface basic sites and acid-base pairs of hydroxyapatite, J. Phys. Chem. C. 118 (2014) 12744–12757, https://doi.org/10.1021/jp500469x.

[15] Y. Li, D. Bahamon, M. Sinnokrot, K. Al-Ali, G. Palmisano, L.F. Vega, Computational modeling of green hydrogen generation from photocatalytic H2S splitting: Overview and perspectives, J. Photochem. Photobiol. C. Photochem. Rev. 49 (2021) 100456, https://doi.org/10.1016/j.jphotochemrev.2021.100456.

[16] G. Rosenman, D. Aronov, L. Oster, J. Haddad, G. Mezinskis, I. Pavlovska, M. Chaikina, A. Karlov, Photoluminescence and surface photovoltage spectroscopy studies of hydroxyapatite nano-Bio-ceramics, J. Lumin. 122–123 (2007) 936–938, https://doi.org/10.1016/j.jlumin.2006.01.331.

[17] Y. Li, D. Bahamon, M. Sinnokrot, L.F. Vega, Computational screening of transition metal-doped CdS for photocatalytic hydrogen production, Npj Comput. Mater. 8 (2022) 229, https://doi.org/10.1038/s41524-022-00922-4.

[18] X. Liu, J. Ma, J. Yang, Visible-light-driven amorphous Fe(III)-substituted hydroxyapatite photocatalyst: Characterization and photocatalytic activity, Mater. Lett. 137 (2014) 256–259, https://doi.org/10.1016/j.matlet.2014.09.018.

[19] V.D. Doan, V.T. Le, T.T.N. Le, H.T. Nguyen, Nanosized zincated hydroxyapatite as a promising heterogeneous photo-fenton-like catalyst for methylene blue degradation, Adv. Mater. Sci. Eng. 2019 (2019) 9, https://doi.org/10.1155/2019/5978149.

[20] C. Wang, Q.Q. Hu, J.Q. Huang, Z.H. Deng, H.L. Shi, L. Wu, Z.G. Liu, Y.G. Cao, Effective water splitting using N-doped TiO2 films: Role of preferred orientation on hydrogen production, Int. J. Hydrog. Energy 39 (2014) 1967–1971, https://doi.org/10.1016/j.ijhydene.2013.11.097.

[21] S. Al Jitan, Y. Li, D. Bahamon, G. Žerjav, V.S. Tatiparthi, C. Aubry, M. Sinnokrot, Z. Matouk, N. Rajput, M. Gutierrez, K. Al-Ali, R. Hashaikeh, A. Pintar, L.F. Vega, G. Palmisano, Unprecedented photocatalytic conversion of gaseous and liquid CO_2 on graphene-impregnated Pt/Cu-TiO2: The critical role of Cu dopant, J. Environ. Chem. Eng. 11 (2023) 109485, https://doi.org/10.1016/j.jece.2023.109485.

[22] S. Lu, H.L. Huynh, F. Lou, M. Guo, Z. Yu, Electrochemical reduction of CO_2 to CH4 over transition metal atom embedded antimonene: First-principles study, J. CO_2 Util. 51 (2021) 101645, https://doi.org/10.1016/j.jcou.2021.101645.

[23] S. Lu, Y. Zhang, F. Lou, Z. Yu, Theoretical study of single transition metal atom catalysts supported on two-dimensional Nb2NO2 for efficient electrochemical CO_2 reduction to CH4, J. CO_2 Util. 62 (2022) 102069, https://doi.org/10.1016/j.jcou.2022.102069.

[24] D. Dos Santos Silva, A.E.C. Villegas, R.D.P.F. Bonfim, V.M.M. Salim, N.S. De Resende, Iron-substituted hydroxyapatite as a potential photocatalyst for selective reduction of CO2with H2, J. CO_2 Util. 63 (2022) 102102, https://doi.org/10.1016/j.jcou.2022.102102.

[25] B. Rego de Vasconcelos, D. Pham Minh, P. Sharrock, A. Nzihou, Regeneration study of Ni/hydroxyapatite spent catalyst from dry reforming, Catal. Today 310 (2018) 107–115, https://doi.org/10.1016/j.cattod.2017.05.092.

[26] N. Umezawa, H.H. Kristoffersen, L.B. Vilhelmsen, B. Hammer, Reduction of CO_2 with water on Pt-loaded rutile TiO2(110) modeled with density functional theory, J. Phys. Chem. C. 120 (2016) 9160–9164, https://doi.org/10.1021/acs.jpcc.5b11625.

[27] G. Kresse, J. Furthmüller, Efficiency of ab-initio total energy calculations for metals and semiconductors using a plane-wave basis set, Comput. Mater. Sci. 6 (1996) 15–50, https://doi.org/10.1016/0927-0256(96)00008-0.

[28] B. Hammer, L.B. Hansen, J.K. Nørskov, Improved adsorption energetics within density-functional theory using revised Perdew-Burke-Ernzerhof functionals, Phys. Rev. B - Condens. Matter Mater. Phys. 59 (1999) 7413–7421, https://doi.org/10.1103/PhysRevB.59.7413.

[29] D. Joubert, From ultrasoft pseudopotentials to the projector augmented-wave method, Phys. Rev. B - Condens. Matter Mater. Phys. 59 (1999) 1758–1775, https://doi.org/10.1103/PhysRevB.59.1758.

[30] J. Heyd, G.E. Scuseria, M. Ernzerhof, Hybrid functionals based on a screened Coulomb potential, J. Chem. Phys. 118 (2003) 8207–8215, https://doi.org/10.1063/1.1564060.

[31] S. Grimme, J. Antony, S. Ehrlich, H. Krieg, A consistent and accurate ab initio parametrization of density functional dispersion correction (DFT-D) for the 94 elements H-Pu, J. Chem. Phys. 132 (2010) 154104, https://doi.org/10.1063/1.3382344.

[32] Y. Bi, S. Ouyang, N. Umezawa, J. Cao, J. Ye, Facet effect of single-crystalline Ag3PO4 sub-microcrystals on photocatalytic properties, J. Am. Chem. Soc. 133 (2011) 6490–6492, https://doi.org/10.1021/ja2002132.

[33] S. Wei, F. Wang, M. Dan, S. Yu, Y. Zhou, Vanadium (V) and Niobium (Nb) as the most promising co-catalysts for hydrogen sulfide splitting screened out from 3d and 4d transition metal single atoms, Int. J. Hydrog. Energy 45 (2020) 17480–17492, https://doi.org/10.1016/j.ijhydene.2020.04.266.

[34] S. Lu, H.L. Huynh, F. Lou, K. Guo, Z. Yu, Single transition metal atom embedded antimonene monolayers as efficient trifunctional electrocatalysts for the HER, OER and ORR: A density functional theory study, Nanoscale 13 (2021) 12885–12895, https://doi.org/10.1039/d1nr02235k.

[35] R. Vasant Kumar, M. Coto, Visible-Light-Active Photocatalysis: Nanostructured Catalyst Design, Mechanisms, and Applications, John Wiley & Sons, 2018, https://doi.org/10.1002/9783527808175.ch18.

[36] K. Kočí, K. Matějů, L. Obalová, S. Krejčíková, Z. Lacný, D. Plachá, L. Čapek, A. Hospodková, O. Šolcová, Effect of silver doping on the TiO2 for photocatalytic reduction of CO_2, Appl. Catal. B Environ. 96 (2010) 239–244, https://doi.org/10.1016/j.apcatb.2010.02.030.

[37] Y. He, Y. Wang, L. Zhang, B. Teng, M. Fan, High-efficiency conversion of CO_2 to fuel over ZnO/g-C3N4 photocatalyst, Appl. Catal. B Environ. 168–169 (2015) 1–8, https://doi.org/10.1016/j.apcatb.2014.12.017.

[38] V. Kumaravel, S. Mathew, J. Bartlett, S.C. Pillai, Photocatalytic hydrogen production using metal doped TiO2: A review of recent advances, Appl. Catal. B Environ. 244 (2019) 1021–1064, https://doi.org/10.1016/j.apcatb.2018.11.080.

[39] Y. Zhu, L. Gong, D. Zhang, X. Wang, J. Zhang, L. Zhang, L. Dai, Z. Xia, Catalytic origin and universal descriptors of heteroatom-doped photocatalysts for solar fuel production, Nano Energy 63 (2019) 103819, https://doi.org/10.1016/j.nanoen.2019.06.015.

[40] Y. Xu, M.A.A. Schoonen, The absolute energy positions of conduction and valence bands of selected semiconducting minerals, Am. Mineral. 85 (2000) 543–556, https://doi.org/10.2138/am-2000-0416.

[41] J. Song, X. Niu, L. Ling, B. Wang, A density functional theory study on the interaction mechanism between H2S and the α-Fe2O3(0001) surface, Fuel Process. Technol. 115 (2013) 26–33, https://doi.org/10.1016/j.fuproc.2013.04.003.

[42] H. Wang, X. Nie, Y. Chen, X. Guo, C. Song, Facet effect on CO_2 adsorption, dissociation and hydrogenation over Fe catalysts: Insight from DFT, J. CO_2 Util. 26 (2018) 160–170, https://doi.org/10.1016/j.jcou.2018.05.003.

[43] N. Almora-Barrios, K.F. Austen, N.H. De Leeuw, Density functional theory study of the binding of glycine, proline, and hydroxyproline to the hydroxyapatite (0001) and (0110) surfaces, Langmuir 25 (2009) 5018–5025, https://doi.org/10.1021/la803842g.

[44] K. Sato, T. Kogure, H. Iwai, J. Tanaka, Atomic-scale {1010} interfacial structure in hydroxyapatite determined by high-resolution transmission electron microscopy, J. Am. Ceram. Soc. 85 (2002) 3054–3058, https://doi.org/10.1111/j.1151-2916.2002.tb00578.x.

[45] Y. Li, D. Bahamon, M. Sinnokrot, L.F. Vega, Insights into the mechanisms of H2S adsorption and dissociation on CdS surfaces by DFT-D3 calculations, Int. J. Hydrog. Energy 48 (2023) 9700–9712, https://doi.org/10.1016/j.ijhydene.2022.12.094.

[46] H. Brasil, A.F.B. Bittencourt, K.C.E.S. Yokoo, P.C.D. Mendes, L.G. Verga, K. F. Andriani, R. Landers, J.L.F. Da Silva, G.P. Valença, Synthesis modification of hydroxyapatite surface for ethanol conversion: The role of the acidic/basic sites ratio, J. Catal. 404 (2021) 802–813, https://doi.org/10.1016/j.jcat.2021.08.050.

[47] B. Averill, P. Eldredge, General chemistry: principles, patterns, and applications , . Chapter 23: The d-Block Elements, Saylor Foundation, 2011.

[48] X. Wang, H. Niu, Y. Liu, C. Shao, J. Robertson, Z. Zhang, Y. Guo, Theoretical investigation on graphene-supported single-atom catalysts for electrochemical CO2reduction, Catal. Sci. Technol. 10 (2020) 8465–8472, https://doi.org/10.1039/d0cy01870h.

[49] H. Zhang, A. Du, Q. Shi, Y. Zhou, Y. Zhang, Y. Tang, Adsorption behavior of CO_2 on pristine and doped phosphorenes: a dispersion corrected DFT study, J. CO_2 Util. 24 (2018) 463–470, https://doi.org/10.1016/j.jcou.2018.02.005.

[50] Y. Zhou, G. Gao, Y. Li, W. Chu, L.W. Wang, Transition-metal single atoms in nitrogen-doped graphenes as efficient active centers for water splitting: A theoretical study, Phys. Chem. Chem. Phys. 21 (2019) 3024–3032, https://doi.org/10.1039/c8cp06755d.

[51] M.A. Raza, F. Li, M. Que, L. Zhu, X. Chen, Photocatalytic reduction of CO2by halide perovskites: Recent advances and future perspectives, Mater. Adv. 2 (2021) 7187–7209, https://doi.org/10.1039/d1ma00703c.

[52] H. Guzmán, M.A. Farkhondehfal, K.R. Tolod, S. Hernández, N. Russo, Photo / electrocatalytic hydrogen exploitation for CO 2 reduction toward solar fuels production, Elsevier Inc,, 2019, https://doi.org/10.1016/B978-0-12-814853-2.00011-4.

[53] R. Chong, Y. Fan, Y. Du, L. Liu, Z. Chang, D. Li, Hydroxyapatite decorated TiO2 as efficient photocatalyst for selective reduction of CO_2 with H2O into CH4, Int. J. Hydrog. Energy 3 (2018) 22329–22339, https://doi.org/10.1016/j.ijhydene.2018.10.045.

[54] X. Chang, T. Wang, J. Gong, CO_2 photo-reduction: Insights into CO_2 activation and reaction on surfaces of photocatalysts, Energy Environ. Sci. 9 (2016) 2177–2196, https://doi.org/10.1039/c6ee00383d.

[55] C.J. Bondue, M. Graf, A. Goyal, M.T.M. Koper, Suppression of hydrogen evolution in acidic electrolytes by electrochemical CO2 reduction, J. Am. Chem. Soc. 143 (2021) 279–285, https://doi.org/10.1021/jacs.0c10397.

[56] J. Wei, Y. Yang, J. Liu, B. Xiong, Design and screening of transition-metal doped chalcogenides as CO_2-to-CO electrocatalysts, J. CO_2 Util. 64 (2022) 102165, https://doi.org/10.1016/j.jcou.2022.102165.

[57] H. Kawanami, Y. Himeda, G. Laurenczy, Chapter Ten - Formic Acid as a Hydrogen Carrier for Fuel Cells Toward a Sustainable Energy System, in: R. van Eldik, C.D.B. T.-A., I.C. Hubbard (Eds.), Inorg. React. Mech., Academic Press, 2017, pp. 395–427, https://doi.org/10.1016/bs.adioch.2017.04.002.

[58] M.T. Tang, H. Peng, P. Schlexer, M. Bajdich, F. Abild-pedersen, From electricity to fuels: descriptors for C1 selectivity in electrochemical CO_2 reduction, Appl. Catal. B Environ. 279 (2020) 119384, https://doi.org/10.1016/j.apcatb.2020.119384.

[59] B. Wei, Y. Xiong, Z. Zhang, J. Hao, L. Li, W. Shi, Efficient electrocatalytic reduction of CO_2 to HCOOH by bimetallic In-Cu nanoparticles with controlled growth facet, Appl. Catal. B Environ. 283 (2021) 119646, https://doi.org/10.1016/j.apcatb.2020.119646.

[60] D. Ren, J. Fong, B.S. Yeo, The effects of currents and potentials on the selectivities of copper toward carbon dioxide electroreduction, Nat. Commun. 9 (2018), https://doi.org/10.1038/s41467-018-03286-w.

[61] J. Wu, Y. Huang, W. Ye, Y. Li, CO_2 reduction: from the electrochemical to photochemical approach, Adv. Sci. 4 (2017) 1700194, https://doi.org/10.1002/advs.201700194.

[62] Y. Wang, Y. Tian, L. Yan, Z. Su, DFT study on sulfur-doped g-C3N4 nanosheets as a photocatalyst for CO_2 reduction reaction, J. Phys. Chem. C. 122 (2018) 7712–7719, https://doi.org/10.1021/acs.jpcc.8b00098.

[63] X. Guan, W. Gao, Q. Jiang, Design of bimetallic atomic catalysts for CO2reduction based on an effective descriptor, J. Mater. Chem. A. 9 (2021) 4770–4780, https://doi.org/10.1039/d0ta11012d.

[64] A.B. Laursen, A.S. Varela, F. Dionigi, H. Fanchiu, C. Miller, O.L. Trinhammer, J. Rossmeisl, S. Dahl, Electrochemical hydrogen evolution: Sabatiers principle and the volcano plot, J. Chem. Educ. 89 (2012) 1595–1599, https://doi.org/10.1021/ed200818t.

[65] E.M. Lopato, E.A. Eikey, Z.C. Simon, S. Back, K. Tran, J. Lewis, J.F. Kowalewski, S. Yazdi, J.R. Kitchin, Z.W. Ulissi, J.E. Millstone, S. Bernhard, Parallelized screening of characterized and DFT-modeled bimetallic colloidal cocatalysts for photocatalytic hydrogen evolution, ACS Catal. 10 (2020) 4244–4252, https://doi.org/10.1021/acscatal.9b05404.

[66] Z. Boukha, M. Kacimi, M.F.R. Pereira, J.L. Faria, J.L. Figueiredo, M. Ziyad, Methane dry reforming on Ni loaded hydroxyapatite and fluoroapatite, Appl. Catal. A Gen. 317 (2007) 299–309, https://doi.org/10.1016/j.apcata.2006.10.029.

[67] J. Thrane, C. Falholt Elvebakken, M. Juelsholt, T. Lindahl Christiansen, K.M. Ø. Jensen, L. Pilsgaard Hansen, L. Fahl Lundegaard, U. Vie Mentzel, M. Thorhauge, A. Degn Jensen, M. Høj, Highly stable apatite supported molybdenum oxide catalysts for selective oxidation of methanol to formaldehyde: structure, activity and stability, ChemCatChem 13 (2021) 4954–4975, https://doi.org/10.1002/cctc.202101220.

[68] Z. Zhang, Z. Yu, K. Feng, B. Yan, Eu3+ doping-promoted Ni-CeO2 interaction for efficient low-temperature CO_2 methanation, Appl. Catal. B Environ. 317 (2022) 121800, https://doi.org/10.1016/j.apcatb.2022.121800.

[69] L. Xue, C. Zhang, J. Wu, Q.Y. Fan, Y. Liu, Y. Wu, J. Li, H. Zhang, F. Liu, S. Zeng, Unveiling the reaction pathway on Cu/CeO2 catalyst for electrocatalytic CO_2 reduction to CH4, Appl. Catal. B Environ. 304 (2022) 120951, https://doi.org/10.1016/j.apcatb.2021.120951.

[70] D. Montalvo, G. Corro, F. Bañuelos, O. Olivares-Xometl, P. Arellanes, U. Pal, Selective alcohols production through CO_2 photoreduction using Co3O4 /TiO2 photocatalyst exploiting synergetic interactions between Ti3+, Co2+ and Co3+, Appl. Catal. B Environ. 330 (2023) 122652 https://doi.org/10.1016/j.apcatb.2023.122652.

[71] L. Collado, P. Reñones, J. Fermoso, F. Fresno, L. Garrido, V. Pérez-Dieste, C. Escudero, M.D. Hernández-Alonso, J.M. Coronado, D.P. Serrano, V.A. de la Peña O'Shea, The role of the surface acidic/basic centers and redox sites on TiO2 in the photocatalytic CO_2 reduction, Appl. Catal. B Environ. 303 (2022), https://doi.org/10.1016/j.apcatb.2021.120931.